






Unraveling of cocatalysts photodeposited selectively on facets of BiVO₄ to boost solar water splitting

Yu Qi^{1,7}, Jiangwei Zhang ^{1,7}, Yuan Kong^{2,7}, Yue Zhao¹, Shanshan Chen ³, Deng Li¹, Wei Liu¹, Yifan Chen⁴, Tengfeng Xie⁴, Junyan Cui⁵, Can Li ^{1✉}, Kazunari Domen ^{3,6} & Fuxiang Zhang ^{1✉}

Bismuth vanadate (BiVO₄) has been widely investigated as a photocatalyst or photoanode for solar water splitting, but its activity is hindered by inefficient cocatalysts and limited understanding of the underlying mechanism. Here we demonstrate significantly enhanced water oxidation on the particulate BiVO₄ photocatalyst via in situ facet-selective photo-deposition of dual-cocatalysts that exist separately as metallic Ir nanoparticles and nano-composite of FeOOH and CoOOH (denoted as FeCoO_x), as revealed by advanced techniques. The mechanism of water oxidation promoted by the dual-cocatalysts is experimentally and theoretically unraveled, and mainly ascribed to the synergistic effect of the spatially separated dual-cocatalysts (Ir, FeCoO_x) on both interface charge separation and surface catalysis. Combined with the H₂-evolving photocatalysts, we finally construct a Z-scheme overall water splitting system using [Fe(CN)₆]^{3-/4-} as the redox mediator, whose apparent quantum efficiency at 420 nm and solar-to-hydrogen conversion efficiency are optimized to be 12.3% and 0.6%, respectively.

¹ State Key Laboratory of Catalysis, Dalian Institute of Chemical Physics, Chinese Academy of Sciences, Dalian 116023, China. ² Hefei National Laboratory for Physical Sciences at the Microscale and Department of Chemical Physics, University of Science and Technology of China, Hefei, Anhui 230026, China. ³ Research Initiative for Supra-Materials (RISM), Shinshu University, 4-17-1 Wakasato, Nagano 380-8553, Japan. ⁴ College of Chemistry, Jilin University, Changchun, Jilin 130012, China. ⁵ School of Material Science and Engineering, Zhengzhou University, No. 100 Science Avenue, Zhengzhou 450001, China. ⁶ Office of University Professors, The University of Tokyo, 7-3-1 Hongo, Bunkyo-ku, Tokyo 113-8656, Japan. ⁷ These authors contributed equally: Yu Qi, Jiangwei Zhang, Yuan Kong. ✉email: canli@dicp.ac.cn; fxzhang@dicp.ac.cn

Particulate photocatalytic overall water splitting (OWS) based on inorganic semiconductor materials with relative good photostability has been demonstrated as one of the most promising ways of realizing scalable and economically viable solar hydrogen production to address energy- and environment-related issues^{1–12}. To achieve high solar-to-hydrogen (STH) energy conversion efficiency, it is necessary to increase the quantum efficiency of photocatalytic OWS over a wide range of wavelengths, particularly the use of visible light^{11,12}. However, extended visible light utilization is generally accompanied by a decreased driving force of the photogenerated carriers to make charge separation extremely difficult. Furthermore, the construction of OWS systems faces serious challenges originating from the sluggish kinetics of water oxidation involving uphill energy barrier and multiple electron transfer¹³. Consequently, visible-light-driven photocatalytic OWS systems are not only limited in number, but also show lower efficiency than those driven by ultraviolet light^{14–19}. Accordingly, it is highly desirable to precisely design and modify photocatalysts with efficient visible light utilization for promotion of water oxidation.

N-type monoclinic bismuth vanadate (BiVO_4) has emerged as one of the most promising visible-light-responsive photocatalysts and photoanodes for water oxidation since Kudo's report in 1998^{20–28}. Owing to its advantages, such as efficient light absorption in the visible light region, good carrier mobility, controllable exposed facets, and non-toxic properties, BiVO_4 semiconductor has been widely and successfully employed as the water oxidation photocatalyst for the assembly of Z-scheme OWS systems using solid conductor (i.e., Au, reduced graphene oxide) or redox couple (i.e., $\text{Fe}^{3+/2+}$, $[\text{Fe}(\text{CN})_6]^{3-/4-}$) as electron mediator^{15,16,29–31}. Specifically, our previous work revealed that the spatial separation of photogenerated electrons and holes can be achieved on the anisotropic facets of BiVO_4 ³², based on which reduction and oxidation cocatalysts are selectively deposited on different facets to remarkably promote its water oxidation and the efficiency of OWS under visible light¹⁶. Although the BiVO_4 photocatalyst has been widely investigated for the assembly of artificial Z-scheme OWS systems, the apparent quantum efficiency (AQE) and STH conversion efficiency achieved so far are still considerably below what is expected. This is mainly due to the shortage of effective cocatalyst regulation and the lack of in-depth understanding of the microscopic mechanisms behind it^{33,34}. Notably, for the assembly of the redox couple-mediated Z-scheme OWS system shown in Fig. 1, the loading of effective cocatalysts is extremely important not only for the acceleration of interfacial electron transfer between the

H_2 -evolving photocatalyst (HEP) and the O_2 -evolving photocatalyst (OEP), but also for the promotion of surface reaction kinetics of water splitting^{35–38}. Therefore, it is a long-term task to develop innovative cocatalysts and unravel their structures as well as influence mechanism on water splitting.

In this study, we address the sluggish water oxidation of BiVO_4 via in situ photodeposition of dual innovative cocatalysts, with emphasis on elucidating the local structures of the cocatalysts and the mechanism of promotion of water oxidation. We demonstrate that the nanocomposite of FeOOH and CoOOH (denoted as FeCoO_x) in situ formed on the {110} facet of BiVO_4 not only lowers Gibbs free energy barrier of water oxidation, but also makes a better promotion on the electron transfer as well as charge separation compared with the commonly used CoO_x cocatalyst. Furthermore, the Ir cocatalyst in situ deposited on the {010} facet of BiVO_4 was found to exhibit superior reduction ability of $[\text{Fe}(\text{CN})_6]^{3-}$ ions to our previously reported Au. Based on the facet-selective loading of the innovative dual-cocatalysts, the evolution rate of O_2 on the BiVO_4 was significantly enhanced, and a particulate Z-scheme OWS system with an AQE of 12.3% at 420 nm and a STH of 0.6%, was finally fabricated using $[\text{Fe}(\text{CN})_6]^{3-/4-}$ as a redox mediator and ZrO_2/TaON or $\text{MgTa}_2\text{O}_{6-x}\text{N}_y/\text{TaON}$ as the HEP. Our results demonstrate the importance and effectiveness of developing suitable cocatalysts for enhancing interfacial charge separation and surface water oxidation kinetics in promoting solar energy conversion.

Results

Structural characterizations of cocatalysts photodeposited. The anisotropic BiVO_4 with exposed {010} and {110} facets was prepared according to our previous study³⁹. The Ir nanoparticles and FeCoO_x nanocomposite were in situ photodeposited on the surface of BiVO_4 from an aqueous solution containing the precursors K_2IrCl_6 , CoSO_4 , and redox $[\text{Fe}(\text{CN})_6]^{3-}$ ions. The as-obtained sample is hereafter denoted as $\text{Ir-FeCoO}_x/\text{BiVO}_4$. As expected from our previous findings on the spatial separation of photogenerated electrons and holes on the anisotropic BiVO_4 ³², the Ir nanoparticles, and FeCoO_x nanocomposite were clearly observed to be selectively deposited on the {010} and {110} facets of BiVO_4 , respectively (Fig. 2a, b). For comparison, the in situ photodeposition of single Ir or CoO_x particles on BiVO_4 was similarly obtained (denoted as Ir/BiVO_4 and $\text{CoO}_x/\text{BiVO}_4$), and the sample was characterized by field-emission scanning electron microscopy (FESEM) to further confirm the facet-selective deposition (Supplementary Fig. 1). It should be noted that the

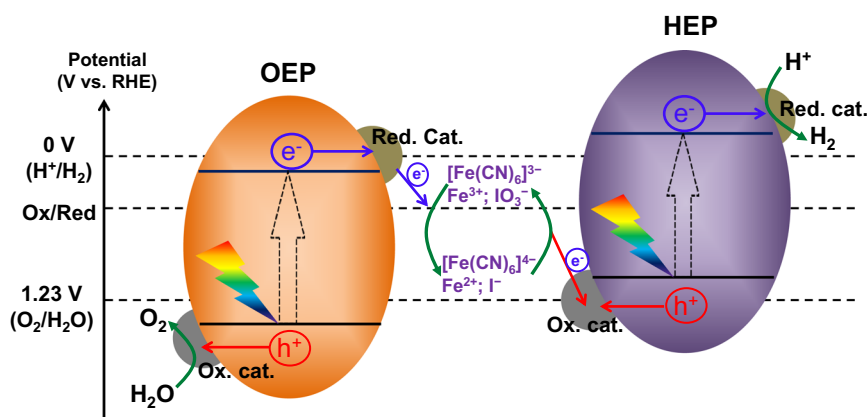


Fig. 1 The energy diagram for a two-step photoexcitation (also called Z-scheme) system with an aqueous redox mediator for overall water splitting. Red. cat.: reduction cocatalyst; Ox. cat.: oxidation cocatalyst; RHE: reversible hydrogen electrode; HEP: H_2 -evolving photocatalyst; OEP: O_2 -evolving photocatalyst.

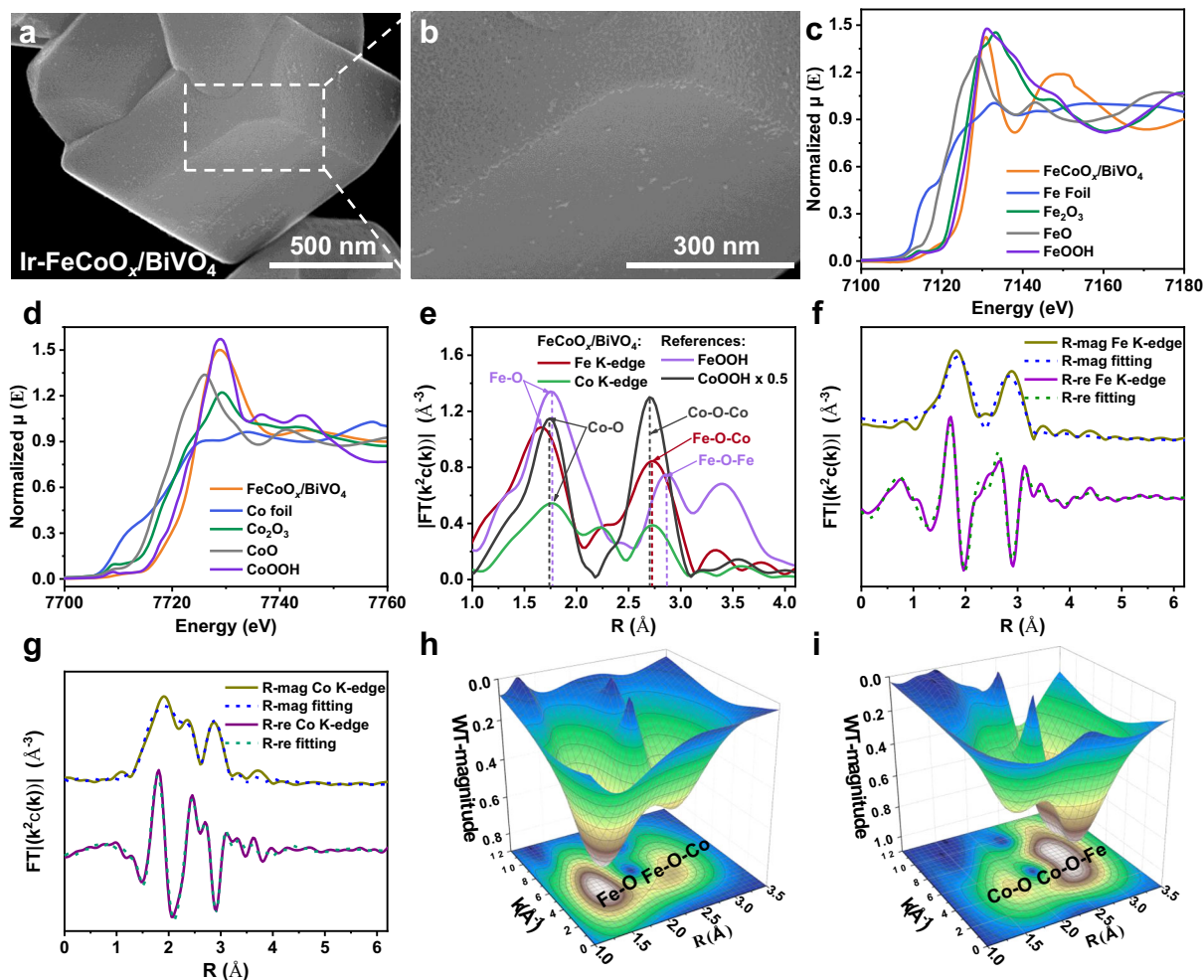


Fig. 2 Morphology and structural characterizations of typical samples. **a, b** FESEM images of the Ir-FeCoO_x/BiVO₄ with different magnification times. **c–i** Structural characterizations of the FeCoO_x/BiVO₄ sample together with references: **c** Normalized Fe K-edge XANES $\mu(E)$ spectra. **d** Normalized Co K-edge XANES $\mu(E)$ spectra. **e** Fe K-edge and Co K-edge radial distance $\chi(R)$ space spectra. **f** Fourier-transformed (FT)-Extended X-ray absorption fine structure (EXAFS) fitting curves at R space of Fe K-edge. **g** FT-EXAFS fitting curves at R space of Co K-edge. **h** Fe K-edge 3D contour wavelet transform. **i** Co K-edge 3D contour wavelet transform.

morphology of the cocatalysts located on the {110} facet of Ir-FeCoO_x/BiVO₄ (Fig. 2b) is clearly different from that of the CoO_x/BiVO₄ sample (Supplementary Fig. 1b), demonstrating the possible interaction between Fe and Co-based compounds. And the change in the long wavelength range of UV-Vis diffuse reflectance spectra (DRS) can confirm the successful deposition of the dual-cocatalysts (Supplementary Fig. 2). The deposited Ir species were verified to exist as metallic Ir nanoparticles by means of X-ray absorption near edge structure (XANES) spectroscopy (Supplementary Fig. 3) and high-resolution transmission electron microscopy image (Supplementary Fig. 4).

To unravel the formation of the FeCoO_x nanocomposite on the {110} facets of BiVO₄, the existing state and dispersion of both Fe and Co elements on FeCoO_x/BiVO₄ (free of Ir nanoparticles) were first analyzed. According to the elemental mapping results shown in Supplementary Fig. 5, both Fe and Co species are similarly located and dispersed, accompanied by the existence of O, which further demonstrates that Co and Fe combine together in the form of oxidation state during the photo-oxidation process. The deposition of Fe should result from redox ions in the reaction solution. The coexistence of both Fe and Co can be further revealed by electron energy loss spectroscopy analysis

(Supplementary Fig. 6). And their oxidation states can be confirmed to be Fe³⁺ and Co³⁺ by the Fe and Co K-edge XANES measurements through comparing with the reference materials (Fig. 2c, d, respectively).

Second, the radial distance space spectra $\chi(R)$ of Fe and Co in FeCoO_x/BiVO₄ and their corresponding references were analyzed, which provides more convincing support for the formation of nanocomposite. As shown in Fig. 2e and Supplementary Fig. 7, the peaks located at approximately 2.72 Å assigned to the Fe–O–Co bond are consistently observed in both the Fe and Co K-edge of the FeCoO_x/BiVO₄ sample, but no scattering path signals attributing to the Co–Co bond (2.41 Å) from Co foil, Fe–Fe bond (2.47 Å) from Fe foil, Co–O–Co bond (2.69 Å) from CoOOH, or Fe–O–Fe bond (2.86 Å) from FeOOH can be observed. This clearly reveals that the formation of nanocomposite is a homogeneous phase of bimetallic hydroxide, instead of single-phase Fe or Co hydroxides. It should be pointed out that the possible nanocomposite of Fe₂O₃ and Co₂O₃ can be ruled out by comparing the fingerprint feature pattern of normalized XANES $\mu(E)$ spectra (Fig. 2c, d and Supplementary Fig. 8a, b) and the first derivative of the normalized XANES $\mu(E)$ spectra (Supplementary Fig. 8c, d). In particular, as shown in Supplementary Fig. 8c, d, the peak positions of FeCoO_x/BiVO₄ are closer

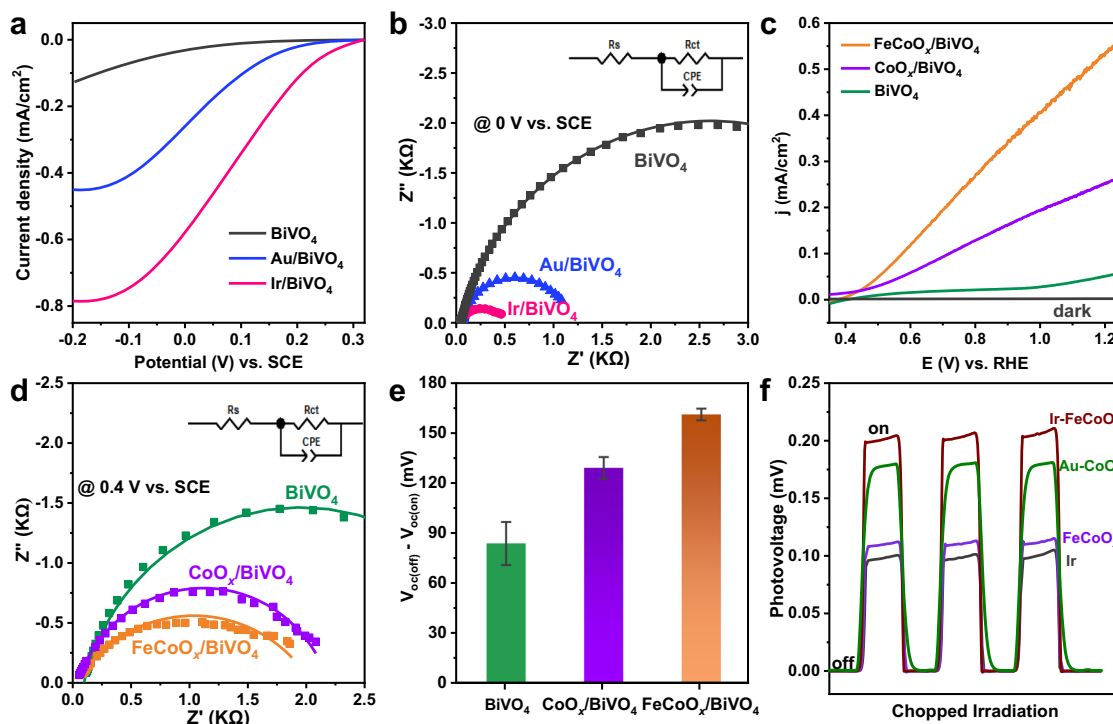


Fig. 3 Electrochemical measurements and characterizations of typical samples. **a** Linear sweep voltammetry curves of typical samples in the 100 mM sodium phosphate buffer solution (pH 6.0) containing 5 mM $K_3[Fe(CN)_6]$. **b** EIS spectra of typical samples in a 100 mM sodium phosphate buffer solution (pH 6.0) containing 5 mM $K_3[Fe(CN)_6]$. SCE, saturated calomel electrode. **c** Photocurrent density-potential curves of $BiVO_4$, $CoO_x/BiVO_4$, and $FeCoO_x/BiVO_4$. **d** EIS spectra of $BiVO_4$, $CoO_x/BiVO_4$, and $FeCoO_x/BiVO_4$ in a 100 mM sodium phosphate buffer solution (pH 6.0). **e** Comparison of difference of OCPs on the $BiVO_4$, $CoO_x/BiVO_4$, and $FeCoO_x/BiVO_4$ under dark and illumination conditions. Measurements were taken at least three times for separate samples and average values are presented with the standard deviation as the error bar. **f** Comparison of promotion effect of cocatalysts on the SPV values of the $BiVO_4$ photocatalyst under chopped visible light irradiation.

to the $FeOOH$ and $CoOOH$ references. Based on these results, the phase species of the $FeCoO_x$ on the surface of $BiVO_4$ sample can be deduced to be more similar to Fe_2O_3/Co_2O_3 . In addition, compared with the corresponding single-phase hydroxides $FeOOH$ and $CoOOH$, $Fe/BiVO_4$ sample exhibits much shorter Fe–O bond and longer Co–O bond, and the length of Co–O–Fe bond is between Co–O–Co and Fe–O–Fe (Fig. 2e). This demonstrates the existence of electron transfer and a strong interaction between Fe and Co in the $FeCoO_x/BiVO_4$ sample, providing further proof about the formation of the nanocomposite.

Third, the formation of the nanocomposite can be further verified by the results of quantitative $\chi(R)$ space spectra fitting and wavelet transform of $\chi(k)$. As seen in Supplementary Table 1, Fe–O–Co bond with similar coordination numbers (Fe–O–Co: 2 at ca. 2.745 Å in Fe K-edge; Co–O–Fe: 2 at ca. 2.761 Å in Co K-edge) can be confirmed. The good fitting results of $\chi(R)$ and $\chi(k)$ space spectra (Fig. 2f, g and Supplementary Fig. 9) with reasonable R-factors and the obtained fitting parameters (Supplementary Table 1) provide a quantitative illustration of the existence of Fe–O–Co bond originating from the nanocomposite structure. As similarly revealed in Fig. 2h, i, the Fe–O–Co bond located at $[\chi(k), \chi(R)]$ of [4.2, 2.74] or Co–O–Fe bond ([6.4, 2.76]) as well as the Fe–O bond ([4.8, 1.64]) or Co–O bond ([4.2, 1.88]) with two scattering path signal can be observed for both Fe and Co K-edge wavelet transform of $\chi(k)$ spectra of $FeCoO_x/BiVO_4$, but the characteristic scattering path signal of Fe–Fe bond ([8.4, 2.52]), Co–Co bond ([7.8, 2.42]), Fe–O–Fe bond ([5.6, 2.82]) or Co–O–Co bond ([6.8, 2.78]) is not observed as similarly as the reference sample (Supplementary Fig. 10).

Effect of reduction and oxidation cocatalysts. As shown in Fig. 1, the water oxidation process of OEP is strongly dependent on both the reduction and oxidation cocatalysts. Therefore, understanding the effect of deposited Ir and $FeCoO_x$ cocatalysts is highly desirable. As depicted in Fig. 3a, the ability of the deposited metallic Ir to reduce $[Fe(CN)_6]^{3-}$ ions was evaluated and found to exhibit a much higher cathode current than that of our previously reported Au nanoparticles on $BiVO_4$ ¹⁶, indicating its superior performance in activating and reducing the $[Fe(CN)_6]^{3-}$ ions. In addition, the deposition of Ir or Au cocatalyst on the surface of $BiVO_4$ can significantly decrease the charge-transfer resistance (R_{ct}) across the semiconductor/electrolyte interface (Fig. 3b), further revealing the effectiveness of the deposited cocatalysts in accelerating the electron transfer from $BiVO_4$ to the $[Fe(CN)_6]^{3-}$ ions (values of R_s and R_{ct} listed in Supplementary Table 2). Meanwhile, the promotion effect of Ir is better than that of Au.

To determine the effect of the $FeCoO_x$ nanocomposite, the efficiencies of charge separation and injection (denoted as η_{sep} and η_{inj} , respectively) on the $FeCoO_x/BiVO_4$ photoanode ($CoO_x/BiVO_4$ and $BiVO_4$ as references) were evaluated by referring to a previous photoelectrochemical analysis²². Figure 3c and Supplementary Fig. 11a show that the current of the $BiVO_4$ photoanode can be remarkably promoted after the deposition of $FeCoO_x$ and CoO_x in both cases, with and without the use of a hole scavenger, among which $FeCoO_x$ exhibits a much better promotion effect than CoO_x . On this basis, both η_{sep} and η_{inj} on the $FeCoO_x/BiVO_4$ photoanode were calculated to be higher than that of the $CoO_x/BiVO_4$ photoanode (Supplementary Fig. 11c, d), demonstrating the better promotion effect of the $FeCoO_x$

nanocomposite on both the separation of photogenerated carriers and the injection of holes into the reaction solution (i.e., surface reaction) with respect to CoO_x . The excellent promotion of FeCoO_x on the surface reaction can be further supported by the electrochemical impedance spectroscopy (EIS) results given in Fig. 3d and Supplementary Table 3, based on which the R_{ct} resistance on the $\text{FeCoO}_x/\text{BiVO}_4$ electrode is the smallest among the three electrodes investigated. On the other hand, the superior promotion effect of FeCoO_x on the charge separation can also be evidenced by its larger open-circuit potential (OCP) on the $\text{FeCoO}_x/\text{BiVO}_4$ compared with $\text{CoO}_x/\text{BiVO}_4$ (Fig. 3e). Based on the previous result that a larger difference of OCPs under dark and illumination conditions corresponds to more intense band bending⁴⁰, therefore the $\text{FeCoO}_x/\text{BiVO}_4$ sample can be deduced to own a more intense band bending than the $\text{CoO}_x/\text{BiVO}_4$ sample, leading to a significantly improved η_{sep} and the more intense band bending should result from the p-n heterojunction between FeCoO_x and BiVO_4 ⁴¹.

Encouraged by the understanding of the functionalities of both reduction and oxidation cocatalysts (i.e., Ir and FeCoO_x), the synergistic effect of dual-cocatalysts on the charge separation was examined using the surface photovoltage (SPV) spectrum. As shown in Fig. 3f, the sample with both Ir and FeCoO_x deposited exhibits a greater SPV amplitude with respect to the sample with single Ir or FeCoO_x loaded. It should be mentioned that a much better promotion effect is also observed for the sample with facet-selective deposition of Ir and FeCoO_x compared to that with facet-selective deposition of Au and CoO_x . These results reveal the importance of both facet-selective deposition of dual-cocatalysts and the development of innovative cocatalysts for maximizing the promotion effect.

Density functional theory calculations on the O_2 -evolving reaction.

Density functional theory (DFT) calculations were performed to further elucidate the microscopic mechanism of the promotion effect of the FeCoO_x cocatalyst on the O_2 -evolving reaction (OER) from the viewpoint of both surface catalysis and interfacial charge transfer. As shown in Fig. 4a–c, the $\text{CoO}_x\text{-FeO}_x\text{-CoO}_x\text{-FeO}_x$ and $\text{CoO}_x\text{-CoO}_x\text{-CoO}_x\text{-CoO}_x$ clusters were simply extracted and placed on the {110} facets of BiVO_4 to simulate the $\text{FeCoO}_x/\text{BiVO}_4$ and $\text{CoO}_x/\text{BiVO}_4$ interfaces, respectively, which origin from the structure of EXAFS measurement. And the schematic of the whole OER mechanism on the $\text{FeCoO}_x/\text{BiVO}_4$ and $\text{CoO}_x/\text{BiVO}_4$ is given in Supplementary Fig. 12 and illustrated in detail in supporting information. Fig. 4d and e presents the Gibbs free energy change diagram of the four elementary steps of OER on the surface of $\text{FeCoO}_x/\text{BiVO}_4$ and $\text{CoO}_x/\text{BiVO}_4$, during which the Co and Fe sites on $\text{FeCoO}_x/\text{BiVO}_4$ were mainly considered as the active sites, respectively. It was demonstrated that the rate-determining step of $\text{FeCoO}_x/\text{BiVO}_4$ (Co or Fe site) and $\text{CoO}_x/\text{BiVO}_4$ is the adsorption of one OH^- to form OOH^* from O^* . The largest decrease of the Gibbs free energy barrier was observed for $\text{FeCoO}_x/\text{BiVO}_4$ (Co site), whereas the OER performance of $\text{FeCoO}_x/\text{BiVO}_4$ (Fe site) is much weaker than that of the corresponding Co site, suggesting that the Co site acts as the main OER site.

Next, we plotted the calculated densities of states (DOS) of the BiVO_4 {110} surface, $\text{CoO}_x/\text{BiVO}_4$ {110} interface, and $\text{FeCoO}_x/\text{BiVO}_4$ {110} interface (Fig. 4f, g, h and Supplementary Fig. 13). Both CoO_x and FeCoO_x are set to be located at the {110} facets of BiVO_4 . For the bare BiVO_4 {110} surface, there is a direct bandgap about 2.1 eV between the valence band and conduction band (Fig. 4f). However, when the $\text{CoO}_x\text{-FeO}_x\text{-CoO}_x\text{-FeO}_x$ cluster is settled on the {110} surface of BiVO_4 , a mixed band mainly composed of Co 3d, Fe 3d, and O 2p states emerges

between the valence band and conduction band (Fig. 4g). It has been demonstrated that the localization of photoexcited holes, as well as subsequent charge separation can be promoted through the formation of mixed bands⁴². In addition, the DOS of the $\text{CoO}_x/\text{BiVO}_4$ {110} interface (Fig. 4h) has no similar result as that of the $\text{FeCoO}_x/\text{BiVO}_4$ {110} interface (Fig. 4g, bandgap = 2.0 eV), implying that the loading of FeCoO_x on BiVO_4 should have better charge separation. In order to microscopically understand the better electron transfer on the FeCoO_x with respect to the CoO_x , their bader charges were calculated and compared. As given in Supplementary Table 4, the changing trend of bader charge on the Co active site after introduction of Fe (increase from 1.2 a.u. in $\text{CoO}_x/\text{BiVO}_4$ to 1.3 a.u. in $\text{FeCoO}_x/\text{BiVO}_4$) is in line with the changing one of experimental valence state (Supplementary Fig. 14). Compared to the $\text{CoO}_x/\text{BiVO}_4$, the higher bader charge on the Co active site in $\text{FeCoO}_x/\text{BiVO}_4$ indicates its stronger oxidation capacity as well as more beneficial electron transfer⁴³. In addition, as shown in Supplementary Fig. 15, the d-band center (Ed) value of Co active sites in $\text{FeCoO}_x/\text{BiVO}_4$ was calculated as -1.63 eV, which is sharply increased with respect to the $\text{CoO}_x/\text{BiVO}_4$ (-2.56 eV). This demonstrates that the electronic structure of Co active sites can be well modulated and optimized in the $\text{FeCoO}_x/\text{BiVO}_4$ due to the introduction of Fe atoms to get much stronger adsorption properties to the OER intermediates according to the d-band center theory^{44,45}. According to previous experimental and theoretical demonstration, the Fe site is relatively inactive during the OER process^{46,47}. So we deduce that the role of Fe is to assist in modifying the geometric and electronic structure of Co in the OER together with our results that very limited contributions of Fe 3d states are observed for the mixed band (Fig. 4g). These conclusions from DFT calculation well match with the aforementioned experimental results.

Photocatalytic performances of Z-scheme OWS. The modified BiVO_4 was employed as an OEP for the assembly of efficient Z-scheme OWS systems together with ZrO_2/TaON or $\text{MgTa}_2\text{O}_{6-x}\text{N}_y/\text{TaON}$ as a HEP under visible light irradiation. The HEPs were prepared and modified with cocatalysts according to previously reported procedures^{16,48,49}, and the diffraction structure and morphology features were coarsely revealed by their powder X-ray diffraction patterns and FESEM images (Supplementary Figs. 16, 17). The contents of deposited Ir and Co on BiVO_4 were optimized to be 0.8 and 0.2 wt%, respectively, via the photocatalytic O_2 evolution reaction (Supplementary Figs. 18, 19). As seen in Fig. 5a, stable evolution curves of H_2 and O_2 with the stoichiometric molar ratio of 2:1 can be observed at the experimental region using the optimized photocatalysts, indicating the successful achievement of the OWS process. Moreover, regardless of using ZrO_2/TaON or $\text{MgTa}_2\text{O}_{6-x}\text{N}_y/\text{TaON}$ as the HEP, similar OWS activities with the initial rates of H_2 and O_2 evolution (ca. 160 and 80 $\mu\text{mol/h}$, respectively) were separately observed, implying that the O_2 evolution on BiVO_4 is the rate-determining step, as similarly observed in our previous study¹⁶. It should be pointed out that when the $\text{Ir-CoO}_x(\text{Imp.})/\text{BiVO}_4$ with Ir and Co randomly impregnated is employed as the OEP, the OWS will not be achieved owing to the significantly decreased O_2 -evolving activity (Supplementary Fig. 20). This indicates the importance of facet-selective deposition of dual-cocatalysts in promoting the O_2 -evolving activity and fabricating a successful OWS system. The multiple cycles of time-course curves shown in Supplementary Figs. 21 and 22 demonstrate the good photostability of the system constructed in this study. The AQE value of OWS as a function of absorption wavelength was found to be in good accordance with the UV-Vis DRS of the OEP and HEP,

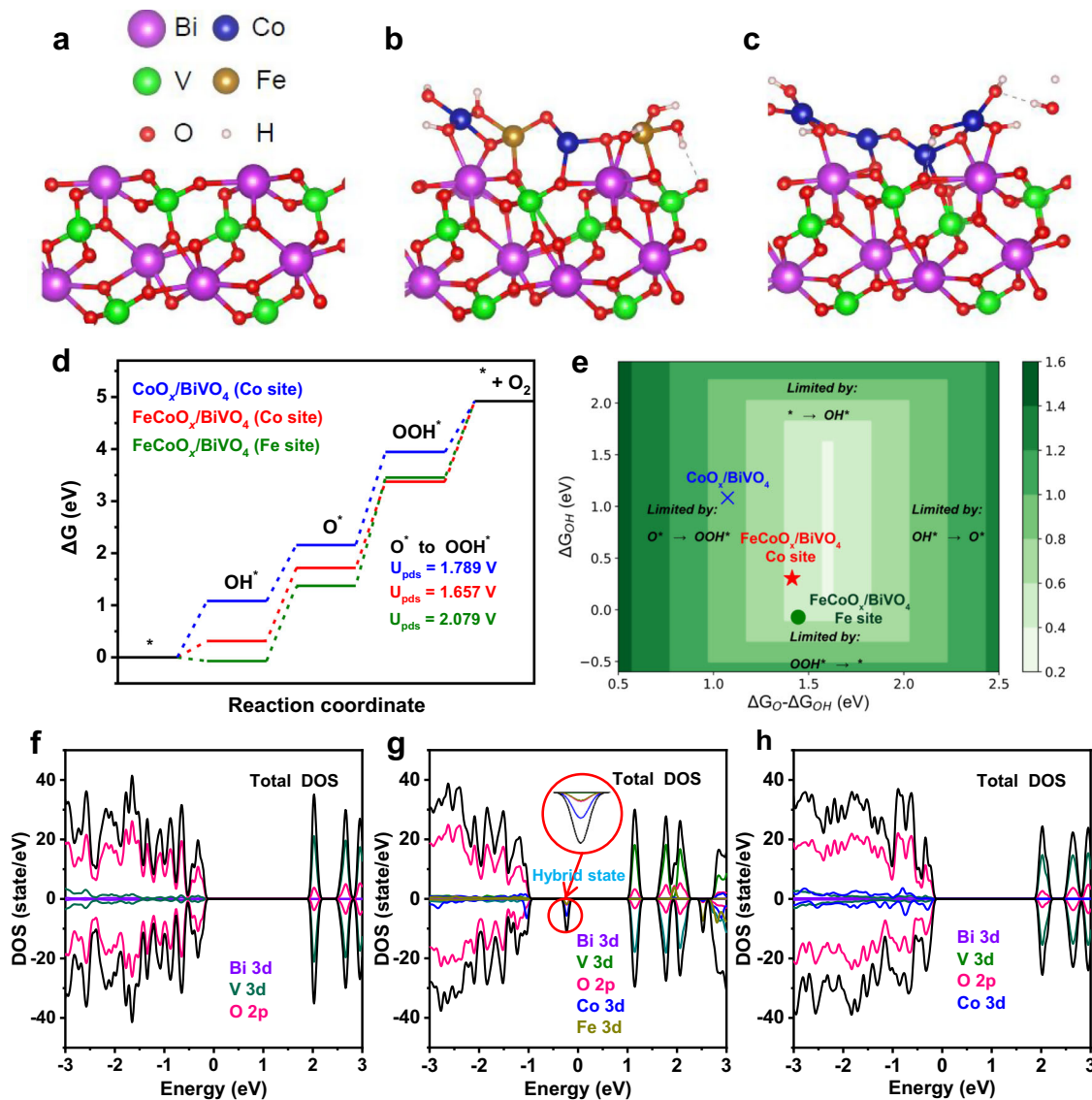


Fig. 4 Theoretical understanding of the promotion effect of the FeCoO_x cocatalyst. Visual representation of structures of BiVO_4 {110} surface (a) $\text{FeCoO}_x/\text{BiVO}_4$ {110} interface (b) and $\text{CoO}_x/\text{BiVO}_4$ {110} interface (c) for the DFT calculations. **d** Free energy diagram for OER process on $\text{FeCoO}_x/\text{BiVO}_4$ and $\text{CoO}_x/\text{BiVO}_4$ {110} interfaces. The surface structures with various reaction intermediates are shown alongside the free energy diagram. U_{pds} , equilibrium potential for the potential determining step. **e** Theoretical overpotential plot with O^* and OH^* binding energies as descriptors. Calculated densities of state for the BiVO_4 {110} surface (f), $\text{FeCoO}_x/\text{BiVO}_4$ {110} interface (g), and $\text{CoO}_x/\text{BiVO}_4$ {110} interface (h).

indicating that the Z-scheme OWS system is driven by visible light excitation (Fig. 5b and Supplementary Fig. 23). The optimal AQE value of OWS at 420 ± 10 nm is 12.3%, and the AQE value at the 500 ± 10 nm is about 3%, demonstrating the wide visible light utilization. According to the activity measurements under the irradiation of AM 1.5 G (Fig. 5c), the STH energy conversion efficiency was calculated to be 0.6%. To the best of our knowledge, both the AQE and STH values should be the highest among the suspending particulate photocatalytic OWS systems using inorganic semiconductor materials with visible light utilization, regardless of one-step or two-step (i.e., Z-scheme) systems.

Discussion

Here, we show a highly efficient Z-scheme OWS system with benchmarked AQE and STH value over particulate inorganic semiconductor photocatalysts with visible light utilization. The success is mainly ascribed to the in situ facet-selective photo-deposition of innovative dual-cocatalysts (Ir nanoparticles and

FeCoO_x nanocomposite), based on which the sluggish water oxidation on BiVO_4 can be largely overcome. Besides the finding and structural unraveling of efficient cocatalysts, the microscopic work mechanism of both reduction and oxidation cocatalysts on the interfacial charge transfer and surface catalysis has been well elucidated respectively. These results should be encouraging and enlightening to the design and assembly of OWS systems for more efficient solar-to-chemical energy conversion.

Methods

Synthesis of modified-TaON and BiVO_4 . ZrO_2 -modified TaON ($\text{Zr}/\text{Ta} = 0.1$) sample and $\text{MgTa}_2\text{O}_{6-x}\text{N}_y/\text{TaON}$ ($\text{Mg}/\text{Ta} = 0.15$) composite were used as the HEPs. The ZrO_2 -modified sample was synthesized by nitridation of the $\text{ZrO}_2/\text{Ta}_2\text{O}_5$ composite and the $\text{MgTa}_2\text{O}_{6-x}\text{N}_y/\text{TaON}$ was prepared by nitridation of the $\text{MgTa}_2\text{O}_6/\text{Ta}_2\text{O}_5$ composite under an ammonia flow (20 mL min^{-1}) at 1123 K for 15 h by referring to the previous works^{48,49}. BiVO_4 was chosen as the OEP, which was similarly synthesized according to our previous hydrothermal process³⁹. Typically, 10 mmol NH_4VO_3 and 10 mmol $\text{Bi}(\text{NO}_3)_3 \cdot 5\text{H}_2\text{O}$ were dissolved in 2.0 M nitric acid solution, whose pH value was then adjusted to be about 0.5 with

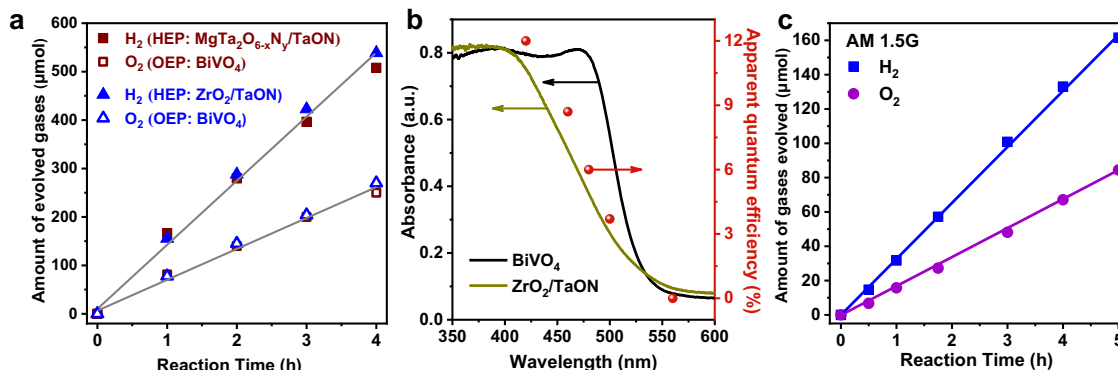


Fig. 5 Photocatalytic activity of Z-scheme OWS. **a** Time course of Z-scheme OWS on the optimized conditions under visible light irradiation. **b** Dependence curve of AQE value as a function of irradiation wavelength, and UV-Vis DRS of the HEP and OEP. **c** Time curve of Z-scheme OWS under illumination of the standard solar simulator (AM 1.5 G, 100 mW cm⁻²). Reaction conditions: **a** 50 mg OEP, 50 mg HEP (ZrO₂/TaON, 1.0 wt% Rh, 1.5 wt% Cr) or 50 mg OEP, 100 mg HEP (MgTa₂O_{6-x}N_y/TaON, 2.5 wt% Rh, 3.75 wt% Cr), 100 mL 25 mM sodium phosphate buffer solution (pH 6.0) containing K₄[Fe(CN)₆] (10 mM), 300 W xenon lamp ($\lambda \geq 420$ nm), temperature: 288 K, Pyrex top-irradiation type. **b** 75 mg OEP, 75 mg HEP (ZrO₂/TaON, 1.0 wt% Rh, 1.5 wt% Cr), 150 mL 25 mM sodium phosphate buffer solution (pH 6.0) containing K₄[Fe(CN)₆] (10 mM), 300 W xenon lamp, temperature: 298 K, Pyrex top-irradiation type. **c** 50 mg OEP, 50 mg HEP (ZrO₂/TaON, 1.0 wt% Rh, 1.5 wt% Cr), 100 mL 25 mM sodium phosphate buffer solution (pH 6.0) containing K₄[Fe(CN)₆] (10 mM), temperature: 288 K, Pyrex top-irradiation type.

ammonia solution (25–28 wt%). The mixed solution was strongly stirred until the observation of a light yellow precipitate that was further aged for about 2 h and then transferred to a Teflon-lined stainless steel autoclave for 10 h hydrothermal treatment at 473 K.

Preparation of Ir/BiVO₄ and CoO_x/BiVO₄. The deposition of Ir or CoO_x on the surface of BiVO₄ was carried out by the photodeposition method. Typically, 0.2 g BiVO₄ powder was dispersed in deionized water containing a calculated amount of K₂IrCl₆ (2.0 wt%) or CoSO₄ (2.0 wt%), and hole (CH₃OH) or electron (NaIO₃) scavenger, separately. The well-mixed solution was then irradiated by 300 W xenon lamp free of any cut-off filter for 2 h. The as-obtained powders after filtration and washing are correspondingly denoted as Ir/BiVO₄ and CoO_x/BiVO₄, which were used for further characterizations and tests.

Preparation of FeCoO_x/BiVO₄ and Ir-FeCoO_x/BiVO₄. Both of the samples were similarly prepared by the in situ photodeposition. Meanwhile, 25 mM phosphate buffer solution (PBS, pH = 6, 50 mL) containing a calculated amount of CoSO₄ and [Fe(CN)₆]³⁻ ions was prepared for the synthesis of FeCoO_x/BiVO₄, while 25 mM phosphate buffer solution (PBS, pH = 6, 50 mL) containing a calculated amount of K₂IrCl₆, CoSO₄ and [Fe(CN)₆]³⁻ ions was prepared for synthesis of Ir-FeCoO_x/BiVO₄.

Preparation of HEP. The deposition of nanoparticulate rhodium-chromium mixed oxides (denoted as Rh_yCr_{2-y}O₃) as a cocatalyst was carried out by the photodeposition method. 0.2 g ZrO₂-modified TaON or MgTa₂O_{6-x}N_y/TaON was dispersed in 20 v% 150 mL methanol solution. A certain amount of Na₃RhCl₆ and K₂CrO₄ (1.0 wt% Rh and 1.5 wt% Cr vs. photocatalyst for ZrO₂/TaON and 2.0 wt% Rh and 3.75 wt% Cr vs. photocatalyst for MgTa₂O_{6-x}N_y/TaON) were added as the precursors. The deposition was carried out under the full-spectral irradiation of 300 W xenon lamp for 6 h. Whereafter, the irradiated solution was centrifuged and washed with distilled water, and then dried at 353 K for overnight to get powder for use.

Preparation of BiVO₄ electrodes. The BiVO₄ photoanode was prepared according to the previous work³⁰. First of all, Bi(NO₃)₃·5H₂O, NH₄VO₃, and polyvinyl alcohol were dissolved in 60% HNO₃ to prepare the precursor solution. Then the precursor solution was spin-coated on the FTO followed by heat treatment at 623 K for 2 h in air to form the BiVO₄ seed layer. Second, the treated FTO was immersed in 2.0 M HNO₃ aqueous solution containing Bi(NO₃)₃·5H₂O and NH₄VO₃, whose pH was adjusted to be 0.9 by adding NH₃·H₂O drop by drop. The formed BiVO₄ precursor film solution was transferred to a Teflon-lined autoclave with the as-prepared substrate for hydrothermal treatment at 473 K for 12 h. The BiVO₄ photoanode film was finally calcined at 773 K for 4 h.

As for the selective deposition of Ir and FeCoO_x cocatalysts on the BiVO₄ photoanode, similar in situ photodeposition method as the powder was adopted. Specifically, the photoanode was immersed in 25 mM phosphate buffer solution (PBS, pH = 6, 50 mL) containing the K₂IrCl₆ or/and CoSO₄ (K₂IrCl₆: 40 μL; CoSO₄: 10 μL, the concentration of solution: 1 mg/mL) and K₃[Fe(CN)₆] (0.5 mM) and irradiated for 3 h. Similarly, CoO_x was photodeposited on the surface of BiVO₄ to prepare the CoO_x/BiVO₄ photoanode.

Measurements of AQE and STH conversion efficiency. The AQE was measured using a Pyrex top-irradiation-type reaction vessel and a 300 W xenon lamp fitted with band-pass filters (ZBPA420, Asahi Spectra Co., FWHM: 10 nm). The number of photons reaching the solution was measured using a calibrated Si photodiode (LS-100, EKO Instruments Co., LTD.), and the AQE (ϕ) was calculated using the following Eq. (1):

$$\phi(\%) = (AR/I) \times 100 \quad (1)$$

where A , R , and I are coefficients, A represents a coefficient (4 for H₂ evolution; 8 for O₂ evolution) and R represents the evolution rate of H₂ or O₂. As measured and calculated, the total number of incident photons at the wavelength of 420, 460, 480, 500, and 560 nm are 8.4×10^{20} , 6.5×10^{20} , 7.1×10^{20} , 4.8×10^{20} , and 6.9×10^{20} photons h⁻¹, respectively. The evolution rates of H₂ on the system containing Rh_yCr_{2-y}O₃-ZrO₂/TaON and Ir-FeCoO_x/BiVO₄ photocatalysts under the wavelength of 420, 460, 480, 500, and 560 nm were tested to be 41.6, 23.0, 17.5, 7.4, and 0 μmol h⁻¹, respectively. The evolution rates of H₂ on the system containing Rh_yCr_{2-y}O₃-MgTa₂O_{6-x}N_y/TaON and Ir-FeCoO_x/BiVO₄ photocatalysts under the wavelength of 420, 460, 480, and 560 nm were tested to be 42.4, 19.0, 9.0, and 0 μmol h⁻¹, respectively.

The STH energy conversion efficiency (η) was calculated according to the following Eq. (2):

$$\eta(\%) = (R_{H_2} \times \Delta G^\circ) / (P \times S) \times 100 \quad (2)$$

where R_{H_2} , ΔG° , P , and S denote the rate of H₂ evolution (mol s⁻¹) in photocatalytic water splitting, standard Gibbs energy of water (237.13×10^3 J mol⁻¹), intensity of simulated sunlight (0.1 W cm⁻²), and irradiation area (4.0 cm²), respectively. The light source was an AM 1.5 G solar simulator (XES-40S2-CE, San-Ei Electric), and a top-irradiation reaction vessel was used. The initial rates of H₂ and O₂ evolution are about 36 and 18 μmol/h, separately.

Photoelectrochemical tests. As for the tests of linear sweep voltammetry (LSV) and EIS, a platinum plate was used as a counter electrode and the saturated calomel electrode (SCE) as the reference electrode. The phosphate buffer solution (pH = 6, 0.1 M) with 5 mM K₃[Fe(CN)₆] aqueous solution and phosphate buffer solution (pH = 6, 0.1 M) were used as the electrolyte. The potential of the working electrode was controlled by a potentiostat (CHI 660E) for the LSV test and potentiostat (Solartron analytic AMETEK) for the EIS test. Before the measurement, the solution was purged with argon gas. The Nyquist plots calculated from EIS were performed from 100,000 to 0.1 Hz. Data were fitted using Zview software.

Current–voltage (J - V) curves under irradiation and darkness were recorded on an electrochemical workstation (CHI 660E). The OCP of photoanode were recorded under illumination and darkness using electrochemical workstation (Solartron analytic AMETEK). A 300 W xenon lamp was used as the light source and the irradiation intensity was high enough to produce a flat band condition of the photoanodes. The electrolyte for J - V curves and OCP was 1 M KBi (pH = 9). 0.2 M Na₂SO₃ was added to the electrolyte as a hole scavenger if necessary.

Data availability

The data that support the findings of this study are available from the source data. Source data are provided with this paper.

Received: 26 April 2021; Accepted: 6 January 2022;

Published online: 25 January 2022

References

- Fujishima, A. & Honda, K. Electrochemical photolysis of water at a semiconductor electrode. *Nature* **238**, 37–38 (1972).
- Lewis, N. S. Toward cost-effective solar energy use. *Science* **315**, 798–801 (2007).
- Kudo, A. & Miseki, Y. Heterogeneous photocatalyst materials for water splitting. *Chem. Soc. Rev.* **38**, 253–278 (2009).
- Chen, X. et al. Semiconductor-based photocatalytic hydrogen generation. *Chem. Rev.* **110**, 6503–6570 (2010).
- Linic, S., Christopher, P. & Ingram, D. B. Plasmonic-metal nanostructures for efficient conversion of solar to chemical energy. *Nat. Mater.* **10**, 911–921 (2011).
- Pinaud, B. A. et al. Technical and economic feasibility of centralized facilities for solar hydrogen production via photocatalysis and photoelectrochemistry. *Energy Environ. Sci.* **6**, 1983–2002 (2013).
- Li, X., Tung, C. & Wu, L. Semiconducting quantum dots for artificial photosynthesis. *Nat. Rev. Chem.* **2**, 160–173 (2018).
- Hisatomi, T. & Domen, K. Reaction systems for solar hydrogen production via water splitting with particulate semiconductor photocatalysts. *Nat. Catal.* **2**, 387–399 (2019).
- Cestellos-Blanco, S. et al. Photosynthetic semiconductor biohybrids for solar-driven biocatalysis. *Nat. Catal.* **3**, 245–255 (2020).
- Kornienko, N. et al. Interfacing nature's catalytic machinery with synthetic materials for semi-artificial photosynthesis. *Nature Nanotech* **13**, 890–899 (2018).
- Wang, Q. & Domen, K. Particulate photocatalysts for light-driven water splitting: mechanisms, challenges, and design strategies. *Chem. Rev.* **120**, 919–985 (2020).
- Kong, D. et al. Recent advances in visible light-driven water oxidation and reduction in suspension systems. *Mater. Today* **21**, 897–924 (2018).
- Bard, A. J. & Fox, M. A. Artificial photosynthesis: solar splitting of water to hydrogen and oxygen. *Acc. Chem. Res.* **28**, 141–145 (1995).
- Fabian, D. M. et al. Particle suspension reactors and materials for solar-driven water splitting. *Energy Environ. Sci.* **8**, 2825–2850 (2015).
- Wang, Q. et al. Scalable water splitting on particulate photocatalyst sheets with a solar-to-hydrogen energy conversion efficiency exceeding 1%. *Nat. Mater.* **15**, 611–615 (2016).
- Qi, Y. et al. Redox-based visible-light-driven Z-scheme overall water splitting with apparent quantum efficiency exceeding 10%. *Joule* **2**, 2393–2402 (2018).
- Maeda, K. et al. Photocatalyst releasing hydrogen from water. *Nature* **440**, 295 (2006).
- Chen, S., Takata, T. & Domen, K. Particulate photocatalysts for overall water splitting. *Nat. Rev. Mater.* **2**, 17050 (2017).
- Takata, T. et al. Photocatalytic water splitting with a quantum efficiency of almost unity. *Nature* **581**, 411–414 (2020).
- Kudo, A. et al. Photocatalytic O₂ evolution under visible light irradiation on BiVO₄ in aqueous AgNO₃ solution. *Catal. Lett.* **53**, 229–230 (1998).
- Kudo, A., Omori, K. & Kato, H. A first aqueous process for preparation of crystal form-controlled and highly crystalline BiVO₄ powder from layered vanadates at room temperature and its photocatalytic and photophysical properties. *J. Am. Chem. Soc.* **121**, 11459–11467 (1999).
- Kim, T. W. & Choi, K. S. Nanoporous BiVO₄ photoanodes with dual-layer oxygen evolution catalysts for solar water splitting. *Science* **343**, 990–994 (2014).
- Kim, J. H. & Lee, J. S. Elaborately modified BiVO₄ photoanodes for solar water splitting. *Adv. Mater.* **31**, 1806938 (2019).
- Luo, W. et al. Solar hydrogen generation from seawater with a modified BiVO₄ photoanode. *Energy Environ. Sci.* **4**, 4046–4051 (2011).
- Abdi, F. F. et al. Efficient solar water splitting by enhanced charge separation in a bismuth vanadate-silicon tandem photoelectrode. *Nat. Commun.* **4**, 2195 (2013).
- Chen, Y. S., Manser, J. S. & Kamat, P. V. All solution-processed lead halide perovskite-BiVO₄ tandem assembly for photolytic solar fuels production. *J. Am. Chem. Soc.* **137**, 974–981 (2015).
- Resasco, J. et al. TiO₂/BiVO₄ nanowire heterostructure photoanodes based on Type II band alignment. *ACS Cent. Sci.* **2**, 80–88 (2016).
- Wang, Q. et al. Molecularly engineered photocatalyst sheet for scalable solar formate production from carbon dioxide and water. *Nat. Energy* **5**, 703–710 (2020).
- Kato, H. et al. Construction of Z-scheme type heterogeneous photocatalysis systems for water splitting into H₂ and O₂ under visible light irradiation. *Chem. Lett.* **33**, 1348–1349 (2004).
- Iwase, A. et al. Reduced graphene oxide as a solid-state electron mediator in Z-scheme photocatalytic water splitting under visible light. *J. Am. Chem. Soc.* **133**, 11054–11057 (2011).
- Pan, L. et al. Boosting the performance of Cu₂O photocathodes for unassisted solar water splitting devices. *Nat. Catal.* **1**, 412–420 (2018).
- Li, R. et al. Spatial separation of photogenerated electrons and holes among {010} and {110} crystal facets of BiVO₄. *Nat. Commun.* **4**, 1432 (2013).
- Yang, J. et al. Roles of cocatalysts in photocatalysis and photoelectrocatalysis. *Acc. Chem. Res.* **46**, 1900–1909 (2013).
- Wang, Y. et al. Mimicking natural photosynthesis: solar to renewable H₂ fuel synthesis by Z-scheme water splitting systems. *Chem. Rev.* **118**, 5201–5241 (2018).
- Sasaki, Y. et al. The effect of co-catalyst for Z-scheme photocatalysis systems with an Fe³⁺/Fe²⁺ electron mediator on overall water splitting under visible light irradiation. *J. Catal.* **259**, 133–137 (2008).
- Maeda, K., Abe, R. & Domen, K. Role and function of ruthenium species as promoters with TaON-based photocatalysts for oxygen evolution in two-step water splitting under visible light. *J. Phys. Chem. C* **115**, 3057–3064 (2011).
- Tabata, M. et al. Modified Ta₃N₅ powder as a photocatalyst for O₂ evolution in a two-step water splitting system with an iodate/iodide shuttle redox mediator under visible light. *Langmuir* **26**, 9161–9165 (2010).
- Ma, S. S. K. et al. Visible-light-driven nonsacrificial water oxidation over tungsten trioxide powder modified with two different cocatalysts. *Energy Environ. Sci.* **5**, 8390–8397 (2012).
- Zhao, Y. et al. A hydrogen farm strategy for scalable solar hydrogen production with particulate photocatalysts. *Angew. Chem. Int. Ed.* **59**, 9653–9658 (2020).
- Li, D. et al. Crystallographic-orientation-dependent charge separation of BiVO₄ for solar water oxidation. *ACS Energy Lett.* **4**, 825–831 (2019).
- Wang, S. et al. New iron-cobalt oxide catalysts promoting BiVO₄ films for photoelectrochemical water splitting. *Adv. Funct. Mater.* **28**, 1802685 (2018).
- Chu, C. et al. Spatially separating redox centers on 2D carbon nitride with cobalt single atom for photocatalytic H₂O₂ production. *Proc. Natl Acad. Sci. USA* **117**, 6376–6382 (2020).
- Zhang, B. et al. High-valence metals improve oxygen evolution reaction performance by modulating 3d metal oxidation cycle energetics. *Nat. Catal.* **3**, 985–992 (2020).
- Norskov, J. K. Chemisorption on metal-surfaces. *Rep. Prog. Phys.* **53**, 1253–1295 (1990).
- Norskov, J. K. Electronic factors in catalysis. *Prog. Surf. Sci.* **38**, 103–144 (1991).
- Zhang, B. et al. Homogeneously dispersed multimetal oxygen-evolving catalysts. *Science* **352**, 333–337 (2016).
- Cheng, W. et al. Lattice-strained metal-organic-framework arrays for bifunctional oxygen electrocatalysis. *Nat. Energy* **4**, 115–122 (2019).
- Chen, S. et al. Efficient visible-light-driven Z-scheme overall water splitting using a MgTa₂O_{6-x}N_y/TaON heterostructure photocatalyst for H₂ evolution. *Angew. Chem. Int. Ed.* **54**, 8498–8501 (2015).
- Maeda, K. et al. Efficient nonsacrificial water splitting through two-step photoexcitation by visible light using a modified oxynitride as a hydrogen evolution photocatalyst. *J. Am. Chem. Soc.* **132**, 5858–5868 (2010).
- Kim, C. et al. (040)-Crystal facet engineering of BiVO₄ plate photoanodes for solar fuel production. *Adv. Energy Mater.* **6**, 1501754 (2016).

Acknowledgements

This work was financially supported by the National Natural Science Foundation of China (21902156, 21925206, 21633009), the National Key R&D Program of China (2020YFA0406102, 2017YFA0204904), the DIPC Foundation of Innovative Research (DIPC I201927), and the Dalian Science and Technology Innovation Fund (2020JJ26GX032). We gratefully acknowledge the BL14W1 beamline of the Shanghai Synchrotron Radiation Facility (SSRF), Shanghai, China, and the 1W1B beamline of the Beijing Synchrotron Radiation Facility (BSRF), Beijing, China for providing the beam time. The numerical calculations in this paper have been done on the supercomputing system in the Supercomputing Center of University of Science and Technology of China.

Author contributions

F.Z. conceived and designed the experiments. Y.Q. carried out most of the preparations, activity test, catalyst characterizations, and wrote the first draft. J.Z. carried out the XAFS measurements and analysis. Y.K. conducted DFT calculation. Y.Z. assisted the synthesis of BiVO₄ photocatalyst. S.C. assisted the synthesis of MgTa₂O_{6-x}N_y/TaON heterostructure photocatalyst. D.L. assisted the synthesis of BiVO₄ photoanode. W.L. conducted the HRTEM and EELS measurements. Y.C. and T.X. conducted the SPV characterizations. F.Z. and C.L. directed the work and revised the manuscript. J.C. gave corrections about DFT calculation part. K.D. instructed synthesis of H₂-evolving photocatalysts and provided useful suggestions and discussion on the EXAFS results. All authors discussed the results and contributed to the manuscript.

Competing interests

The authors declare no competing interests.

Additional information

Supplementary information The online version contains supplementary material available at <https://doi.org/10.1038/s41467-022-28146-6>.

Correspondence and requests for materials should be addressed to Can Li or Fuxiang Zhang.

Peer review information *Nature Communications* thanks Krishnan Rajeshwar and the other, anonymous, reviewer(s) for their contribution to the peer review of this work. Peer reviewer reports are available.

Reprints and permission information is available at <http://www.nature.com/reprints>

Publisher's note Springer Nature remains neutral with regard to jurisdictional claims in published maps and institutional affiliations.



Open Access This article is licensed under a Creative Commons Attribution 4.0 International License, which permits use, sharing, adaptation, distribution and reproduction in any medium or format, as long as you give appropriate credit to the original author(s) and the source, provide a link to the Creative Commons license, and indicate if changes were made. The images or other third party material in this article are included in the article's Creative Commons license, unless indicated otherwise in a credit line to the material. If material is not included in the article's Creative Commons license and your intended use is not permitted by statutory regulation or exceeds the permitted use, you will need to obtain permission directly from the copyright holder. To view a copy of this license, visit <http://creativecommons.org/licenses/by/4.0/>.

© The Author(s) 2022